

Supplementary Information

Ti₃C₂ MXene as the “energy band bridge” to regulate the heterointerface mass transfer and electrons reversible exchange process for Li-S batteries

Ruohan Hou^{a, b} †, Shijie Zhang^{a, b, c} †, Peng Zhang^{a, b, c*}, Yongshang Zhang^{a, b, c}, Neng Li^d, ZuHao Shi^d, Guosheng Shao^{a, b, c*}

a. *School of Materials Science and Engineering, Zhengzhou University, Zhengzhou 450001, China.*

b. *State Center for International Cooperation on Designer Low-carbon & Environmental Materials (CDLCEM), Zhengzhou University, Zhengzhou 450001, China.*

c. *Zhengzhou Materials Genome Institute (ZMGI), Zhongyuanzhigu, Building 2, Xingyang 450100, China.*

d. *State Key Laboratory of Silicate Materials for Architecture, Wuhan University of Technology, Wuhan 430070, PR China*

*Corresponding author: zhangp@zzu.edu.cn; gsshao@zzu.edu.cn

† These authors contributed equally to this work.

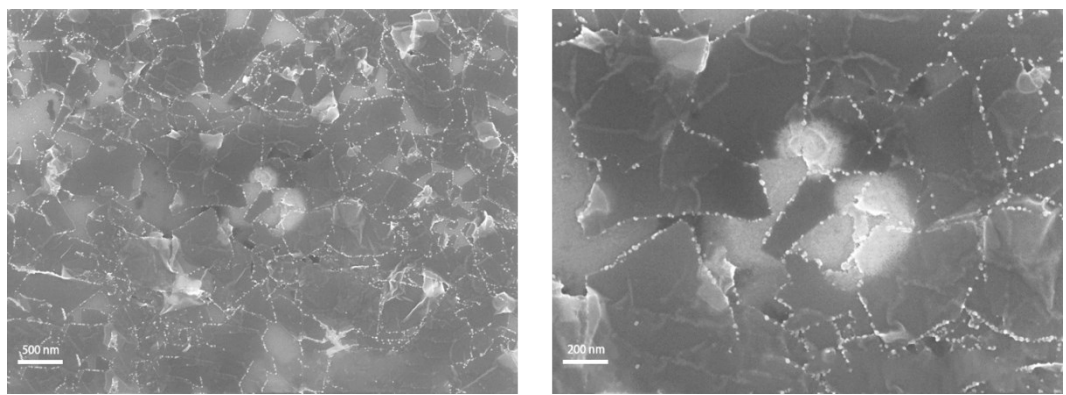


Figure. S1 SEM images of delaminated $\text{Ti}_3\text{C}_2\text{T}_x$ MXene flakes

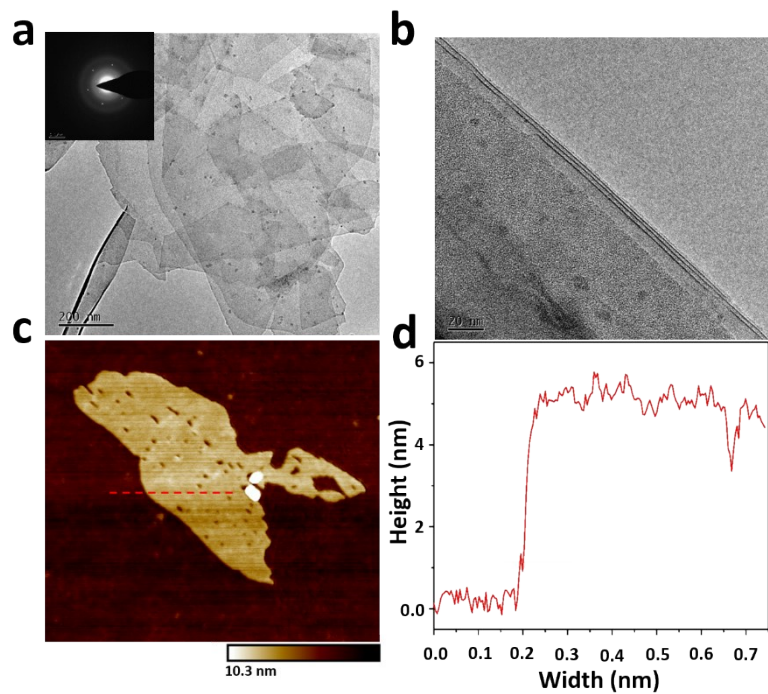


Figure. S2 (a, b) TEM for delaminated $\text{Ti}_3\text{C}_2\text{T}_x$ MXene and inset being the electron diffraction pattern from. (c, d) Atomic force microscopy (AFM) micrographs of the MXene flakes.

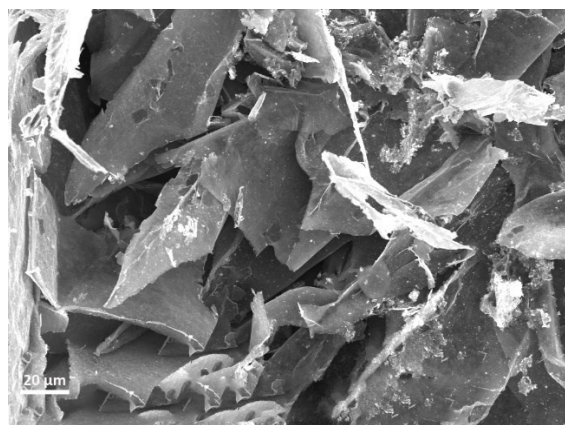


Figure. S3 SEM image of freeze-drying gel-like $\text{Ti}_3\text{C}_2\text{T}_x$ ($\text{g-}\text{Ti}_3\text{C}_2\text{T}_x$) MXene.

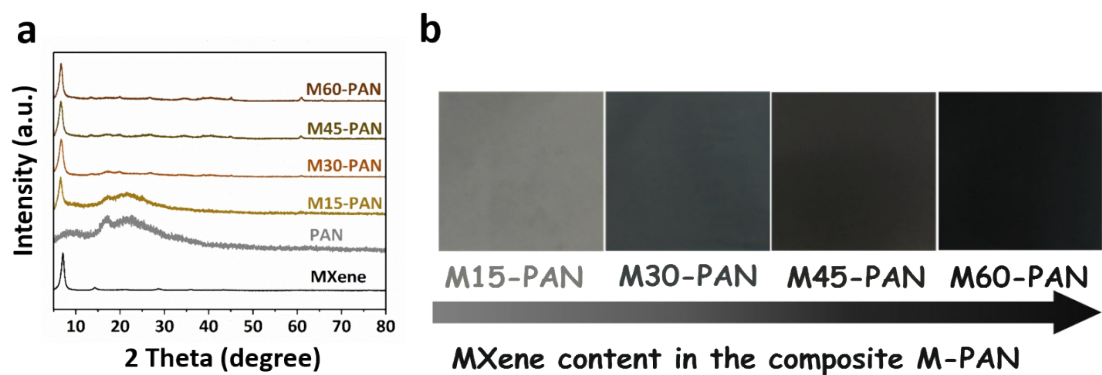


Figure. S4 (a) XRD patterns of the M-PAN with different MXene contents, (b) Optical images of the M-PAN composite.

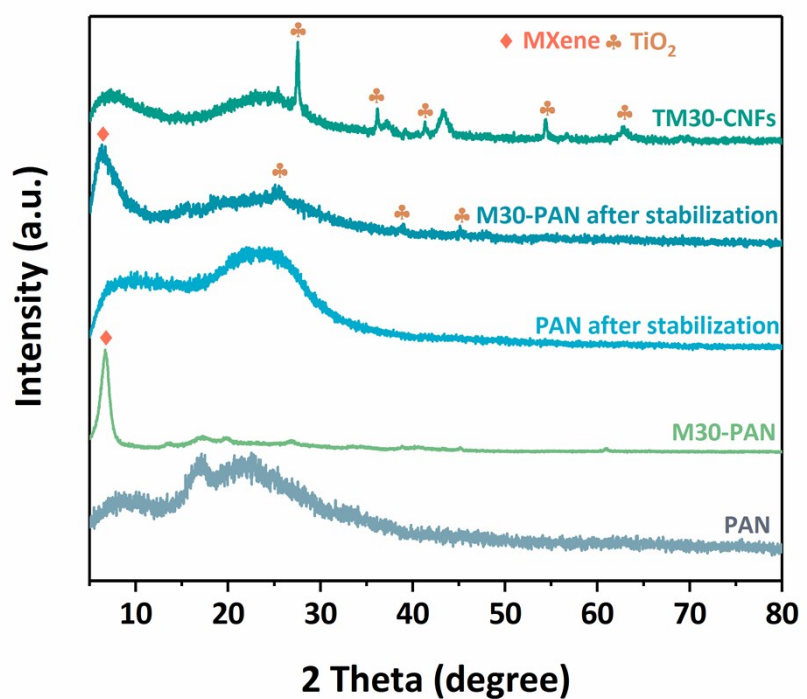


Figure. S5 XRD patterns of the as-electrospun PAN, M30-PAN, M30-PAN after stabilization and TM-30CNFs.

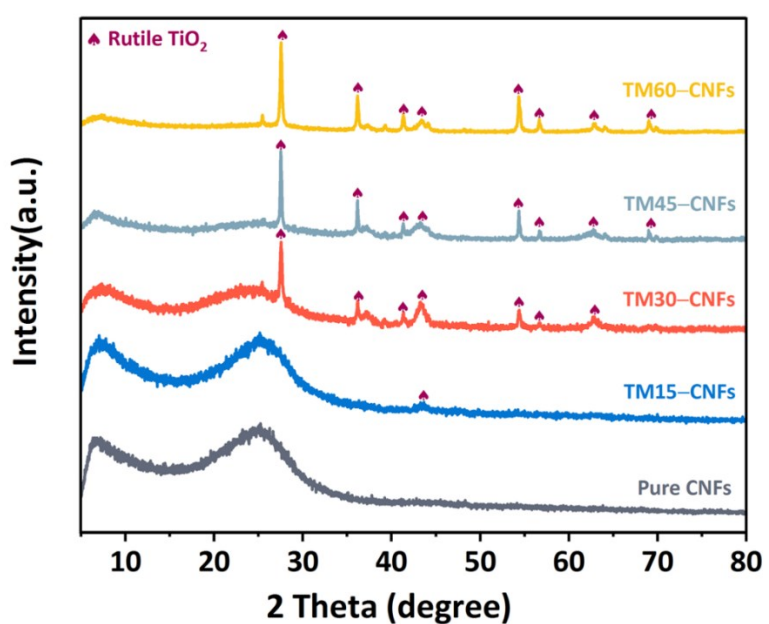


Figure. S6 XRD patterns of pure CNFs and TM-CNFs.

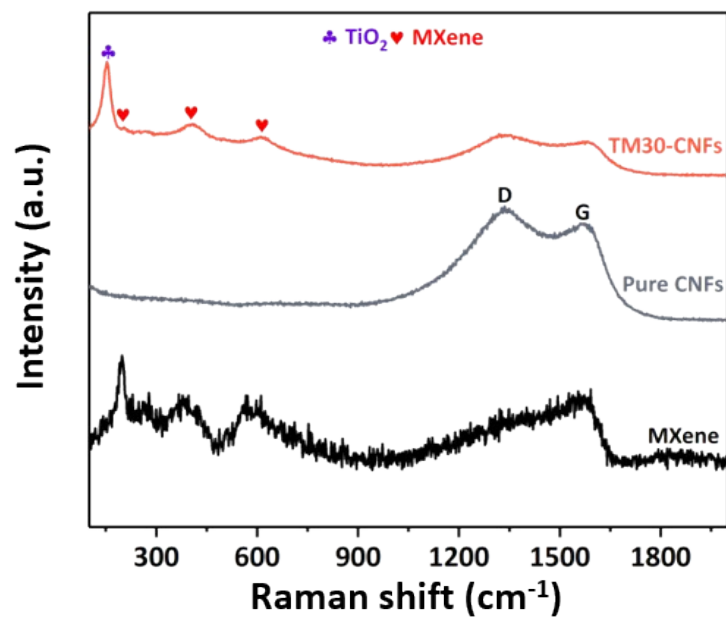


Figure. S7 Raman spectroscopy of MXene, pure CNFs and TM30-CNFs.

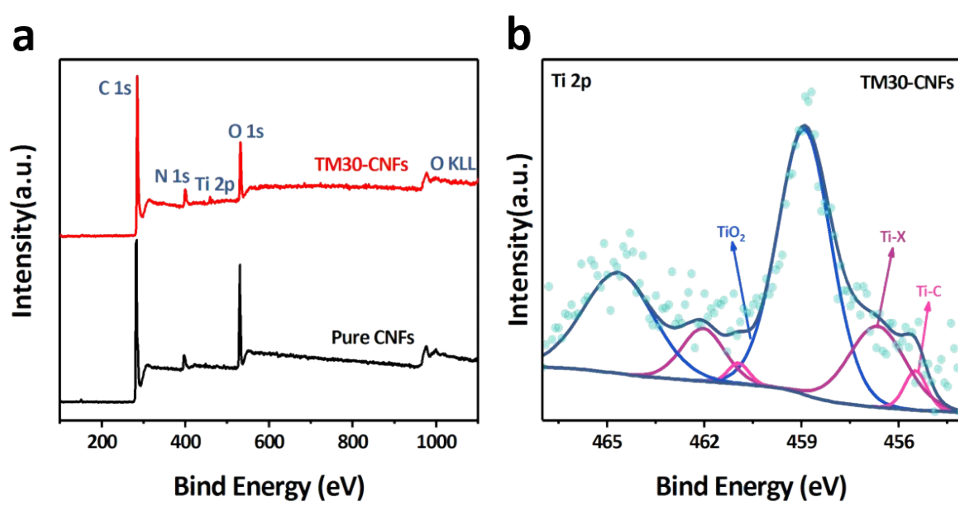


Figure. S8 (a) Survey XPS spectrum of TM30-CNFs, CNFs, (b) Ti 2p spectrum of TM30-CNFs.

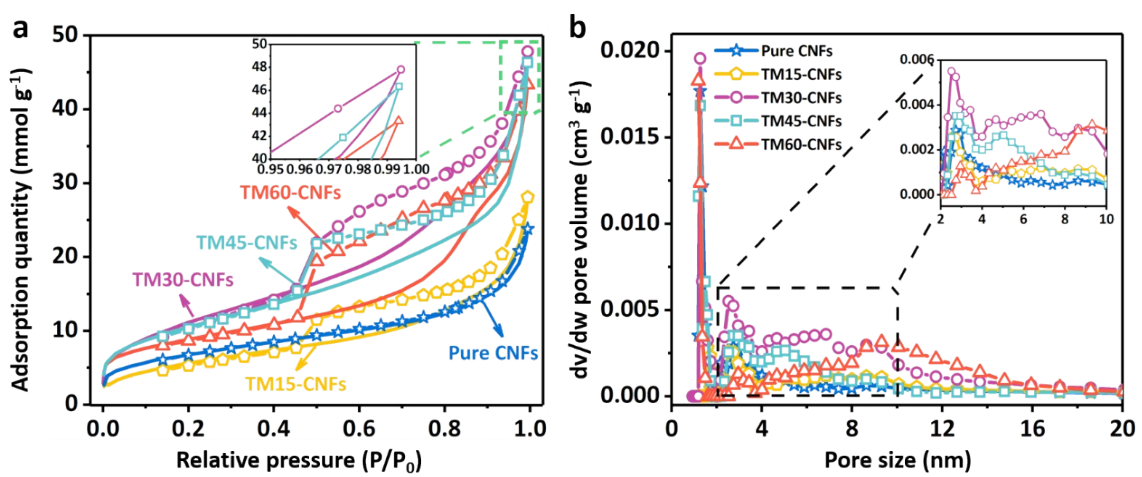


Figure. S9 (a) Nitrogen adsorption and desorption isotherms, and (b) pore size distributions of Pure CNFs and TM-CNFs.

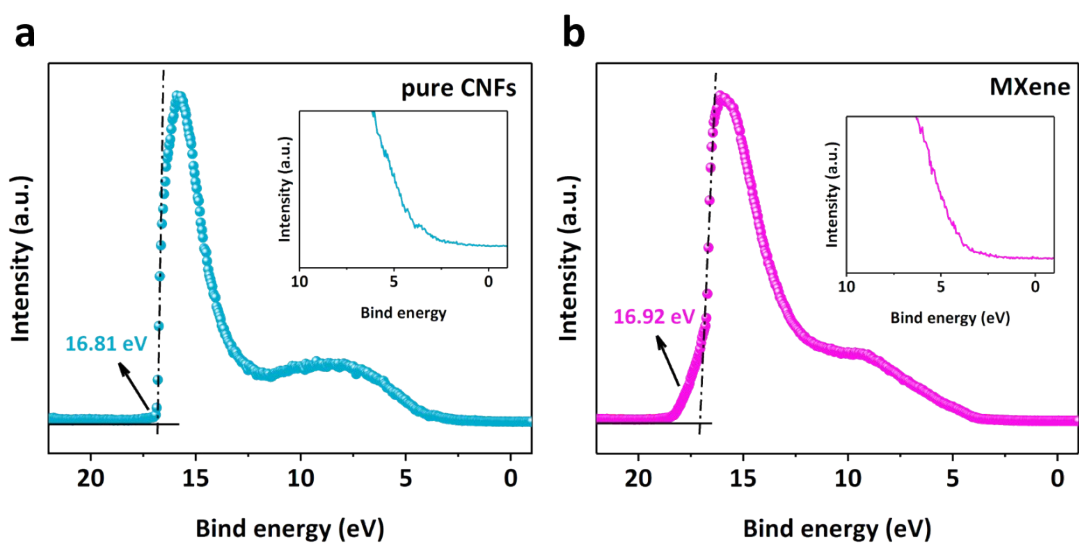


Figure. S10 Survey UPS spectrum of pure CNFs and MXene with insert the UPS valence band spectra of pure CNFs and MXene.

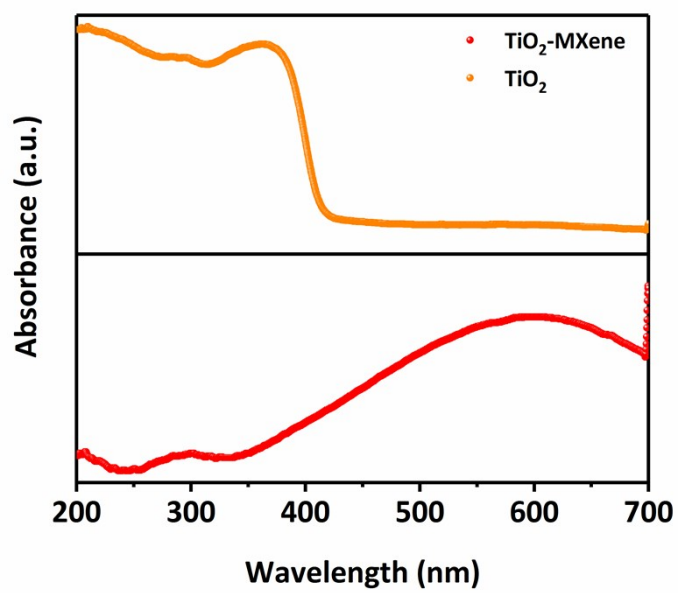


Figure. S11 UV-vis DRS of TiO_2 and TiO_2 -MXene.

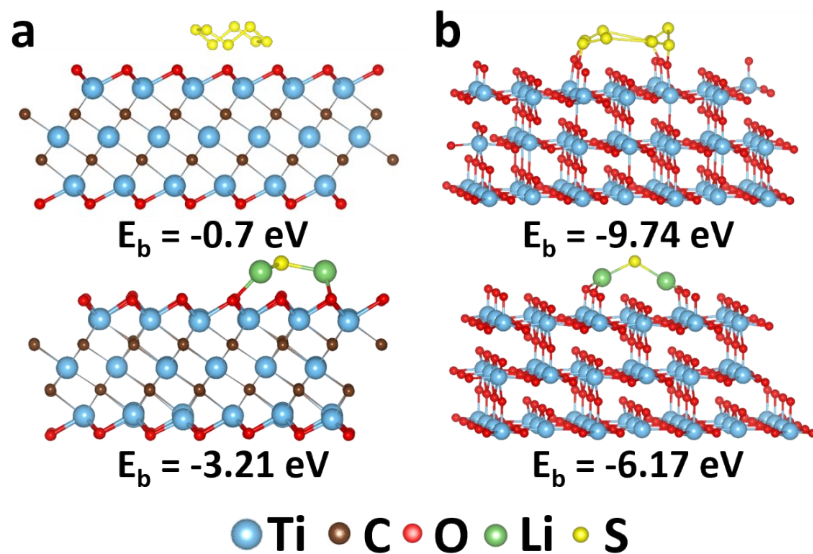


Figure. S12 The optimal configurations of S_8 and Li_2S adsorbed on the (a) $Ti_3C_2T_x$ and (b) TiO_2 respectively.

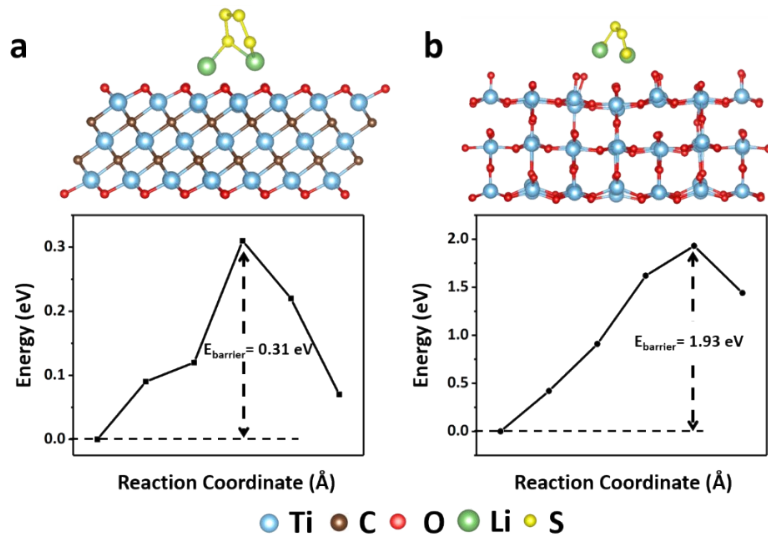


Figure. S13 The geometrical configurations of Li_2S_4 diffusion along the [001] direction on the substrate surface of (a). MXene, and (b). TiO_2 , with the related energy profile for Li_2S_4 migration along the [001].

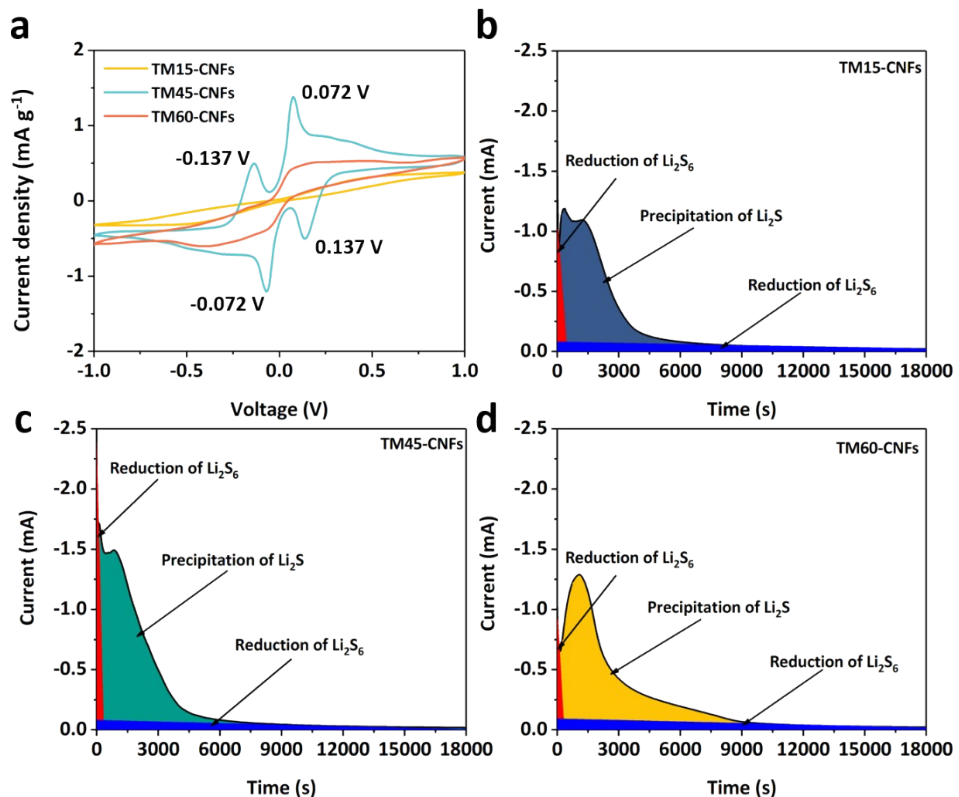


Figure. S14 (a) CV profiles of symmetrical Li_2S_6 - Li_2S_6 cells assembly with TM15-CNFs, TM45-CNFs and TM60-CNFs at the sweep rate of 0.5 mV s^{-1} . (b-c) Potentiostatic discharge profiles of the cells with TM15-CNFs, TM45-CNFs and TM60-CNFs based electrodes at 2.05 V .

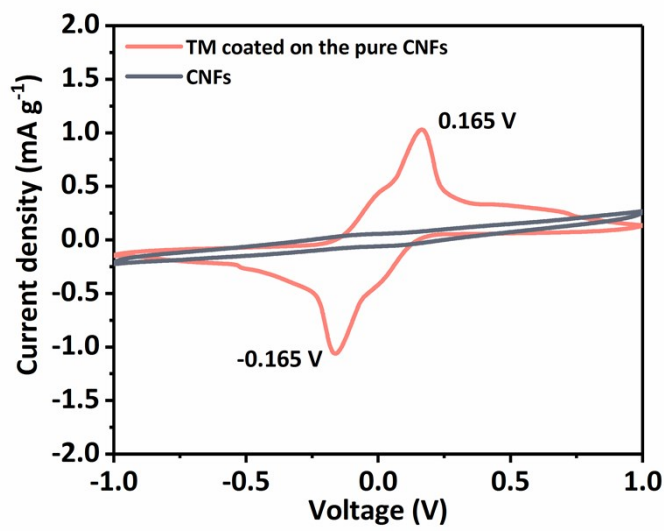


Figure. S15 CV profiles of symmetrical Li_2S_6 - Li_2S_6 cells assembly with TM coated on the CNFs at the sweep rate of 0.5 mV s^{-1} .

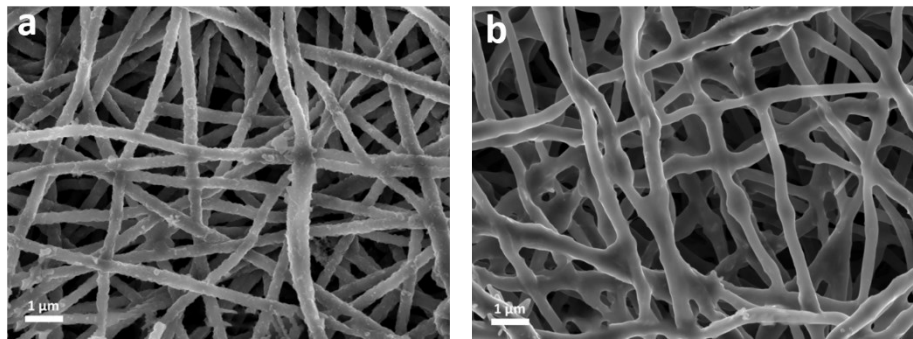


Figure. S16 The SEM images of Li₂S deposition on the (a) CNFs, and (b) TM30-CNFs.

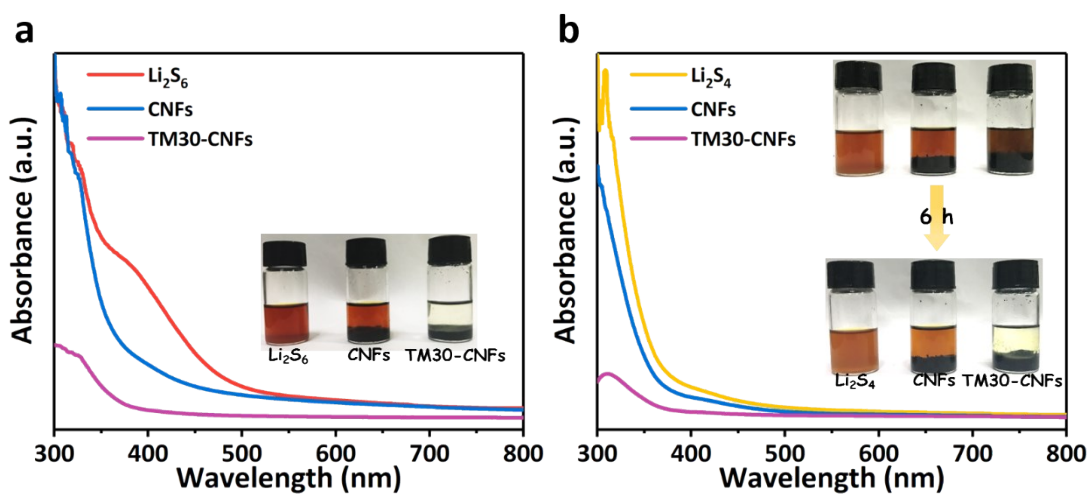


Figure. S17 (a) The UV-vis spectra of CNFs and TM30-CNFs after soaking in the Li_2S_6 solution for 6 h; (b) the digital photos and UV-vis spectra of CNFs and TM30-CNFs after soaking in the Li_2S_4 solution for 6 h.

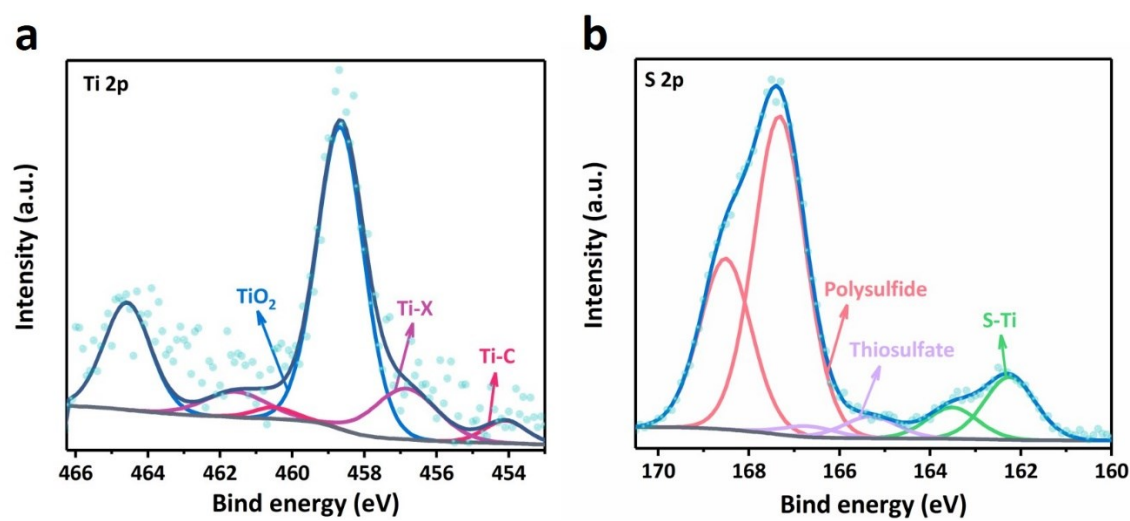


Figure. S18 (a) Ti 2p and (b) S 2p spectrum of the TM30-CNFs after LiPS adsorption.

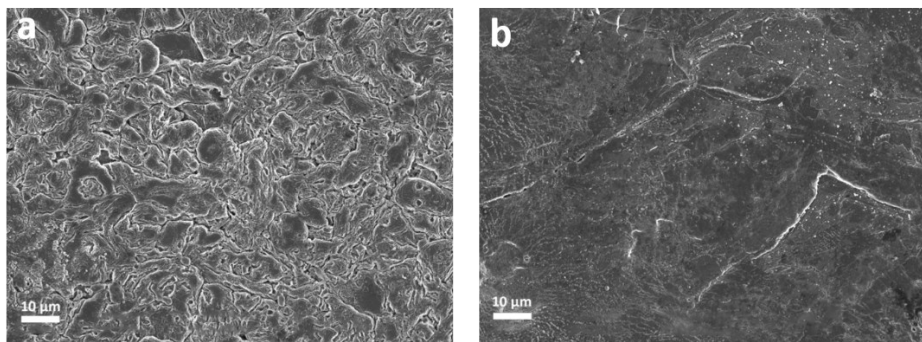


Figure. S19 The SEM images of lithium anode for the cells with (a) CNFs and (b) TM30-CNFs cathodes after 20 cycles.

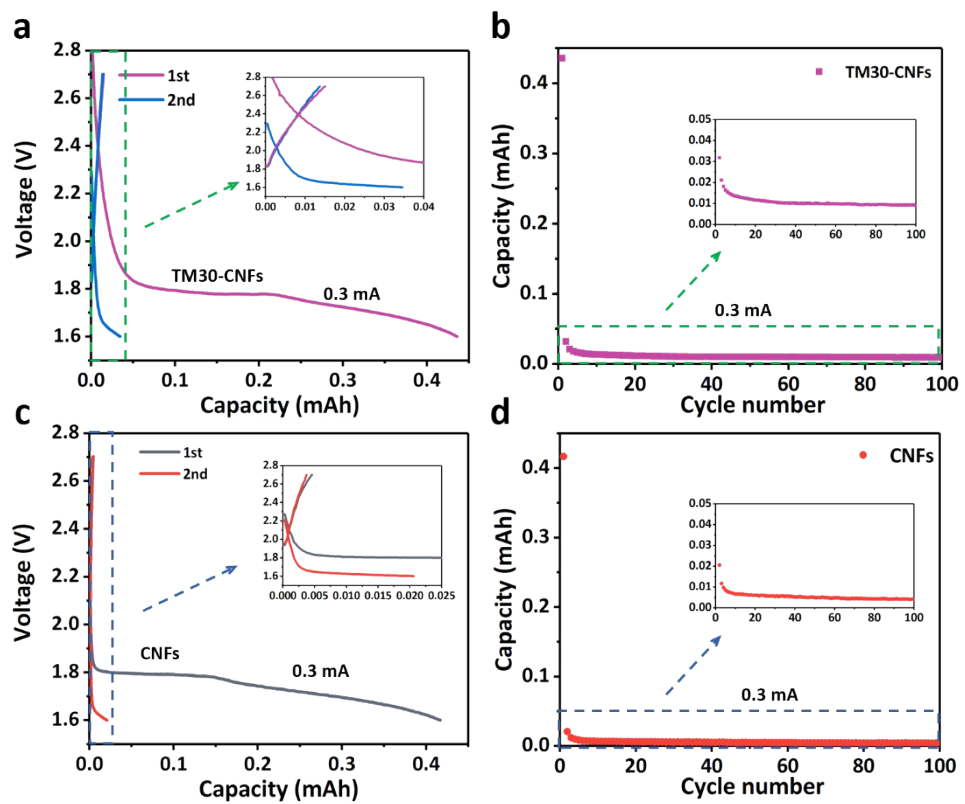


Figure. S20 (a), (c) Galvanostatic charge/discharge profiles of TM30-CNFs and CNFs half-cell at 0.3 mA;(b), (d) Cycling performances of TM30-CNFs and CNFs based cathodes half-cell at 0.3 mA.

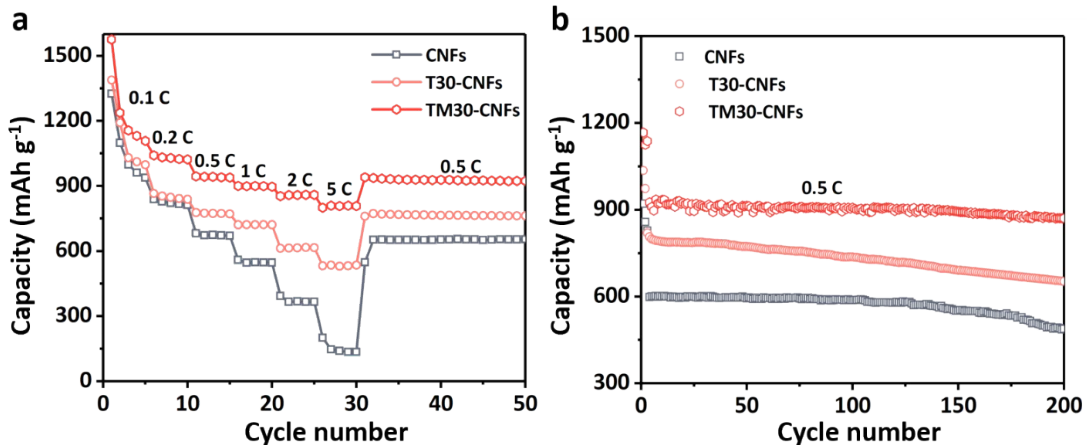


Figure. S21 (a) Rate performance of T30-CNFs, TM30-CNFs and CNFs based cathodes from 0.1 C to 5 C rates., (b) Cycling performances of T30-CNFs, TM30-CNFs and CNFs based cathodes at 0.5 C (with 2 cycles at 0.1 C for activation)

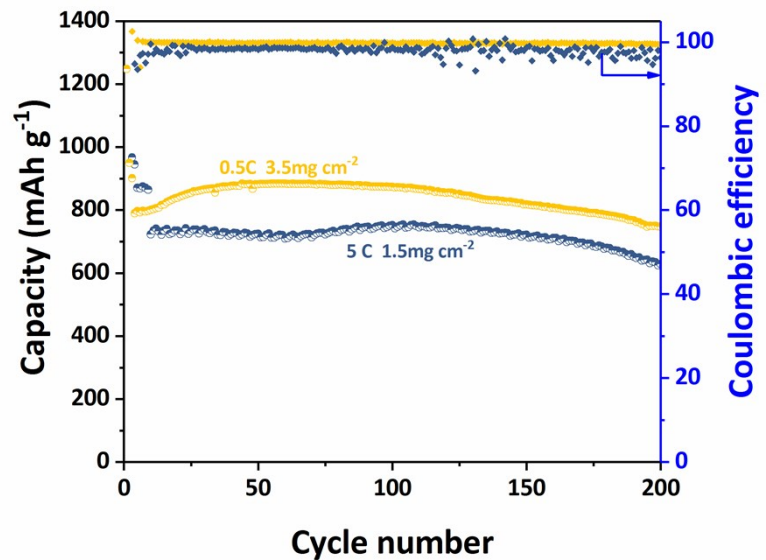


Figure. S22 Cycling performances of TM30-CNFs cathode with sulfur area mass loading 3.5 mg cm^{-2}

and 1.5 mg cm^{-2} at 0.5 C and 5 C respectively.

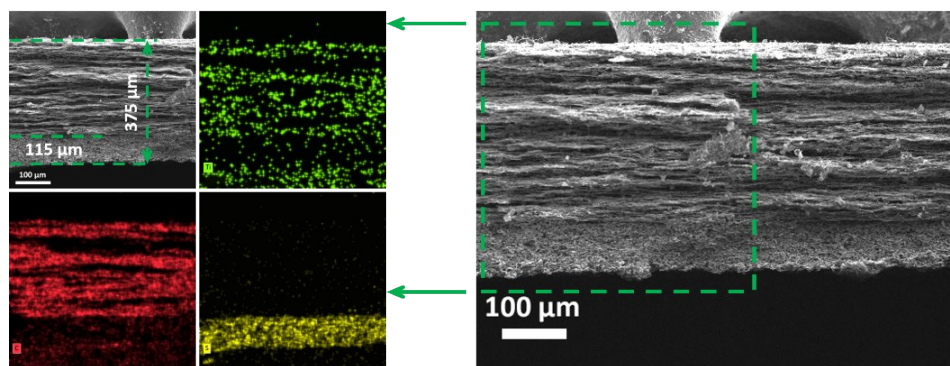


Figure. S23 The SEM cross-section image of TM30-CNFs cathode under 10.5mg^{-2} loading and related element mapping (Titanium, Carbon and Sulfur).

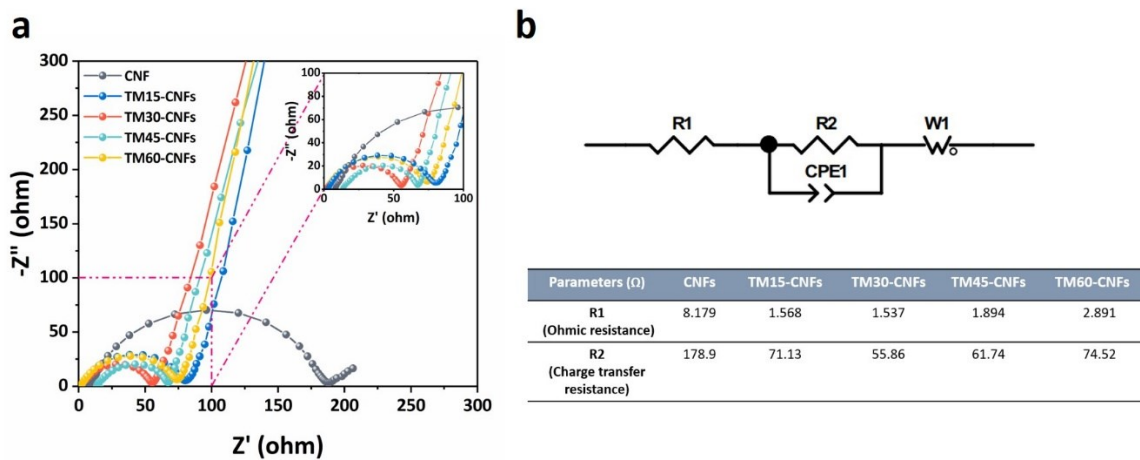


Figure. S24 (a) Electrochemical impedance spectroscopy curves of pure CNFs and TM-CNFs

cathodes, (b) Equivalent circuit diagram and corresponding fitting results.

Where R_1 denotes ohmic resistance, R_2 and CPE_1 represent the charge transfer resistance and relative double layer capacitance, and W_1 is the Warburg impedance relating to a combination of diffusional effects of lithium-ions.

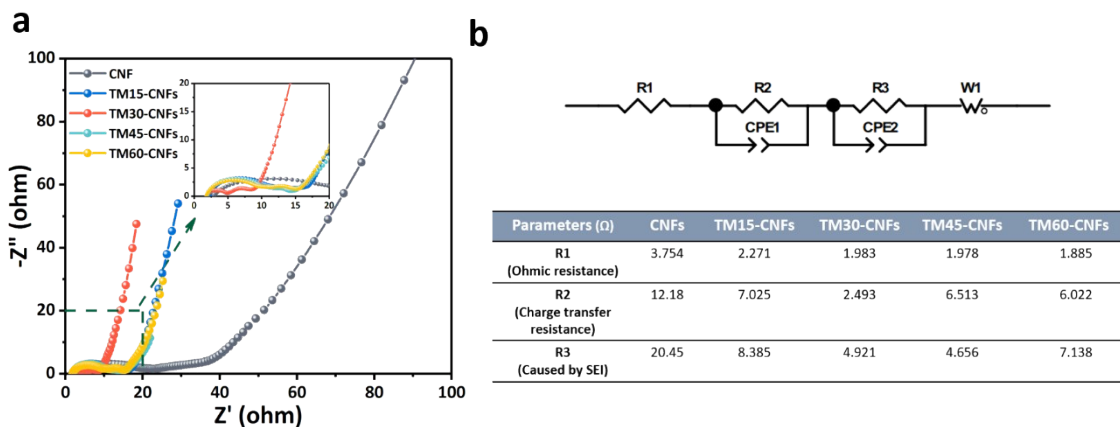


Figure. S25 (a) Electrochemical impedance spectroscopy curves of pure CNFs and TM-CNFs cathodes after 20 cycles at 0.5 C, (b) equivalent circuit model and related results required for analyzing the impedance spectra.

Where R1 denotes ohmic resistance, R2 and CPE1 represent the charge transfer resistance and relative double layer capacitance, R3 and CPE2 are the resistance and capacitance of the SEI film formed at the electrode surface, and W1 is the Warburg impedance relating to a combination of diffusional effects of lithium-ions.

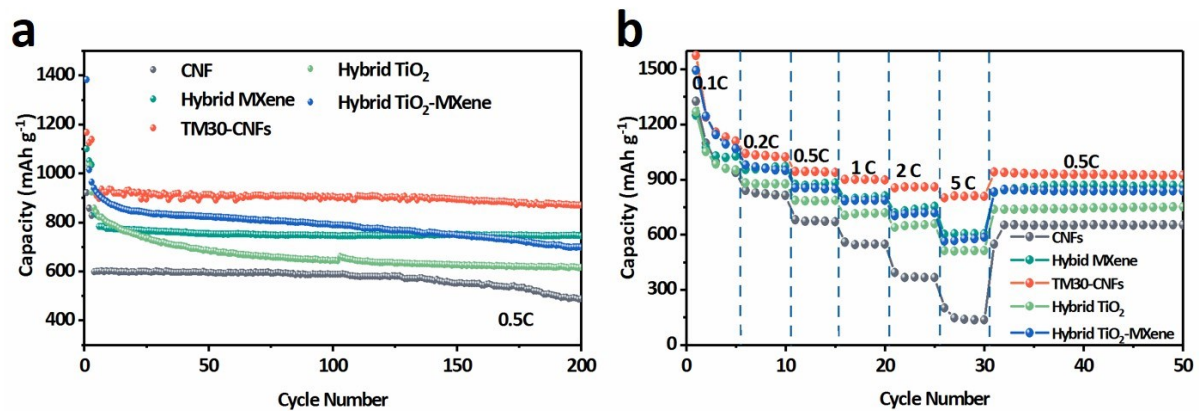


Figure. S26 (a) Cycling performances of pure CNFs, Hybrid MXene, Hybrid TiO₂, Hybrid TiO₂-MXene and TM30-CNFs at 0.5 C, (b) Rate performance of pure CNFs, TM30-CNFs, Hybrid TiO₂, Hybrid MXene and Hybrid TiO₂-MXene cathodes from 0.1 C to 5 C rates.

and TM30-CNFs at 0.5 C, (b) Rate performance of pure CNFs, TM30-CNFs, Hybrid TiO₂, Hybrid MXene and Hybrid TiO₂-MXene cathodes from 0.1 C to 5 C rates.

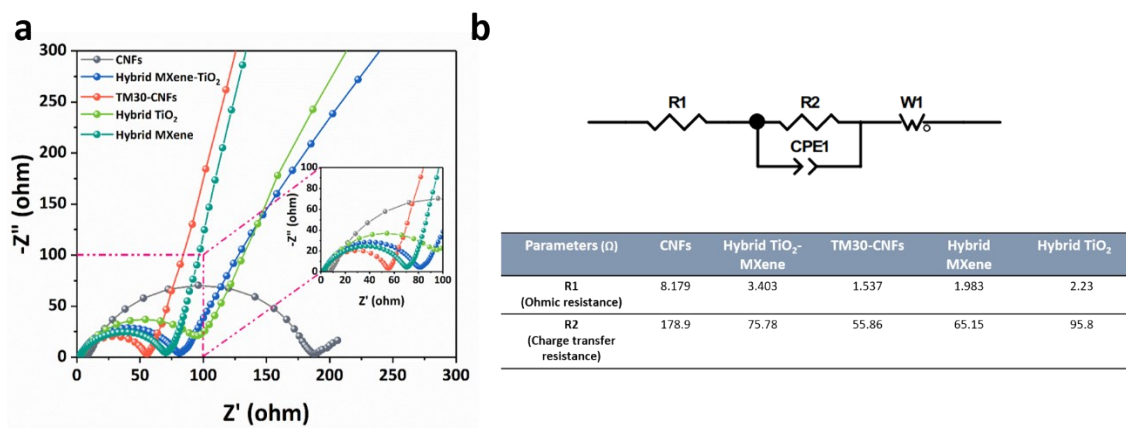


Figure. S27 (a) Electrochemical impedance spectroscopy curves of pure CNFs, TM30-CNFs, Hybrid TiO₂, Hybrid MXene and Hybrid MXene-TiO₂ cathodes, (b) Impedance spectrum related equivalent circuit and analysis results.

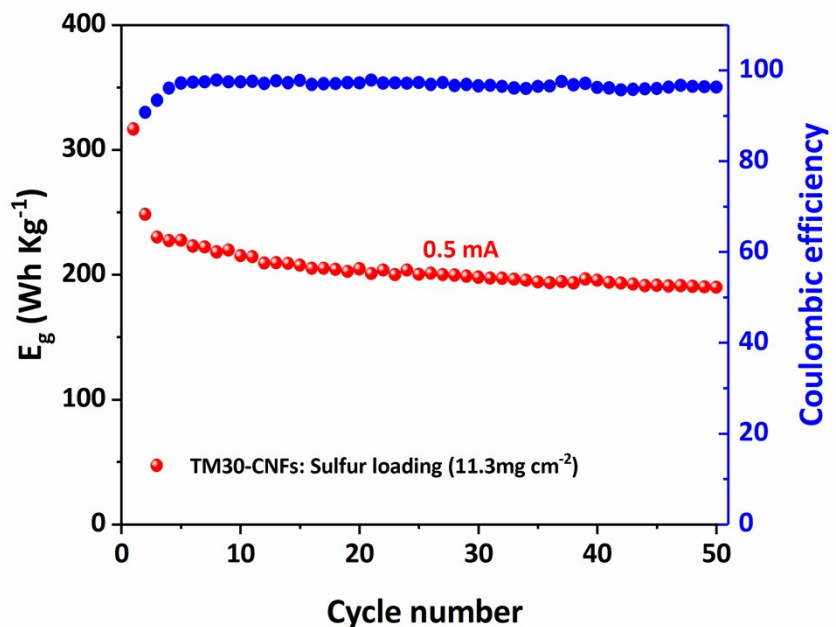


Figure. S28 Cycling property at 0.5 mA with high areal mass loading (11.3 mg cm^{-2}) of TM30-CNFs.

The full-cell gravimetric energy density of the jelly roll was evaluated basis of the coin-cell data using follow equation ¹:

$$E_g = V C / \sum m_i$$

where the E_g is the full-cell gravimetric (Wh kg^{-1}), V is the average working voltage (2.10 V is assumed for Li-S batteries), C is the areal discharge capacity (mAh cm^{-2}), and m_i is the mass of per unit square (mg cm^{-2}), including the sulfur loading (11.3 mg cm^{-2}), TM30-CNFs current collector (8.3 mg cm^{-2}), PP separator (1.12 mg cm^{-2}), Li metal (12.5 mg cm^{-2}) anode, and electrolyte ($\rho \approx 1.1 \text{ mg cm}^{-3}$, $64 \mu\text{L}$).

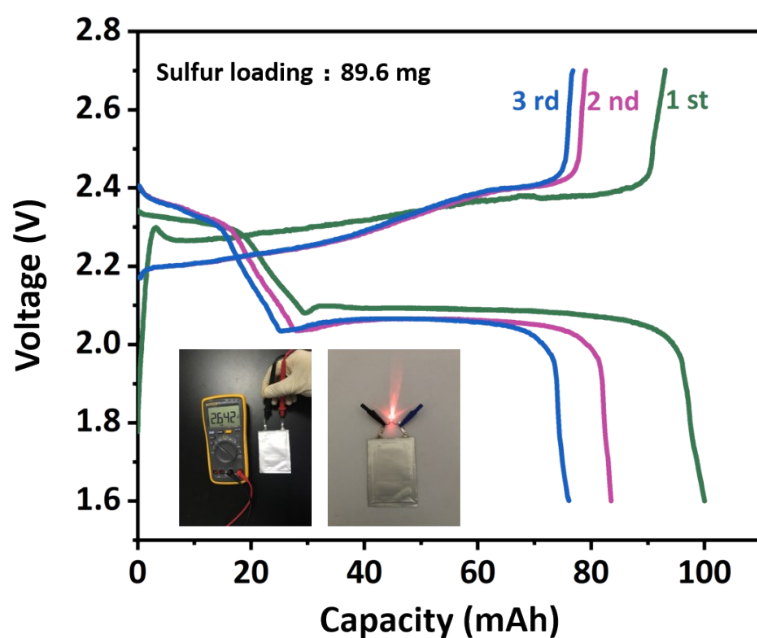


Figure. S29 The pouch cell assembled with TM30-CNFs cathode power the LEDs, and Galvanostatic charge/discharge profiles at 2 mA.

Table S1 Electrochemical performance of various sulfur host materials for Li-S battery

Sample	Mass loading (mg cm ⁻²)	Electrochemical performance	Reference
MXene/CNT	5.5	5mAh cm ⁻² , 910mAh g ⁻¹ at 0.2C(the 1st).	²
Ti ₃ C ₂ Nanoribbon	0.7-1	1062mAh g ⁻¹ at 0.2 C (the 1st), 611mAh g ⁻¹ after 50 cycles at 0.5C.	³
Ni-doped MXene	5.1	588mAh g ⁻¹ after 500 cycles at 0.2C.	⁴
S/Ti ₂ C	1	1090mAh g ⁻¹ at 0.5 C (the 1st) .	⁵
MXene/1T-2H	2-4	1194.7mAh g ⁻¹ at 0.1 C (the 1st).	⁶
MoS ₂ -C			
CNT@TiO _{2-x}	8.6	5.4mAh cm ⁻² ,625mAh g ⁻¹ after 100 cycles at 0.05C.	⁷
S@TiO ₂ /Ti ₂ C	1.8-2.0	844mAh g ⁻¹ after 100 cycles at 0.2 C.	⁸
MNSs@d-Ti ₃ C ₂	1.2	1140 mAh g ⁻¹ at 0.05 C (the 1st).	⁹
Ti ₃ C ₂ @PDA	1.5	1197 mAh g ⁻¹ at 0.5 C (the 1st).	¹⁰
MXene/RGO aerogels	6	5.27 mAh cm ⁻² , 879 mAh g ⁻¹ after 30 cycles at 0.1 C.	¹¹
TiO ₂ -MXene/C 3D network	1.5-2 10.5/11.3	870.2 mAh g⁻¹ at 0.5 C after 200 cycles, 723.3 mAh g⁻¹ at 1C after 500 cycles. 10.85 mAh cm⁻², 916 mAh g⁻¹ at 0.05 C; Full-cell energy density 316.7 Wh Kg⁻¹ at 0.5 mA.	This work

References

- 1 W. J. Xue, Z. Shi, L. M. Suo, C. Wang, Z. Q. Wang, H. Z. Wang, K. P. So, A. Maurano, D. W. Yu, Y. M. Chen, L. Qie, Z. Zhu, G. Y. Xu, J. Kong and J. Li, *Nat. Energy*, 2019, **4**, 374-382.
- 2 X. Liang, Y. Rangom, C. Y. Kwok, Q. Pang and L. F. Nazar, *Adv. Mater.*, 2016, **29**, 1603040.
- 3 Y. F. Dong, S. H. Zheng, J. Q. Qin, X. J. Zhao, H. D. Shi, X. H. Wang, J. Chen and Z. S. Wu, *ACS Nano*, 2018, **12**, 2381-2388.
- 4 W. Z. Bao, L. Liu, C. Y. Wang, S. Choi, D. Wang and G. X. Wang, *Adv. Energy Mater.*, 2018, **8**, 1702485.
- 5 X. Liang, A. Garsuch and L. F. Nazar, *Angew. Chem.*, 2015, **54**, 3907-3911.
- 6 Y. L. Zhang, Z. J. Mu, C. Yang, Z. K. Xu, S. Zhang, X. Y. Zhang, Y. J. Li, J. P. Lai, Z. H. Sun, Y. Yang, Y. G. Chao, C. J. Li, X. X. Ge, W. X. Yang and S. J. Guo, *Adv. Funct. Mater.*, 2018, **28**, 1707578.
- 7 Y. K. Wang, R. F. Zhang, J. Chen, H. Wu, S. Y. Lu, K. Wang, H. L. Li, C. J. Harris, K. Xi, R. V. Kumar and S. J. Ding, *Adv. Energy Mater.*, 2019, **9**, 1900953.
- 8 C. Du, J. Wu, P. Yang, S. Y. Li, J. M. Xu and K. X. Song, *Electrochim. Acta*, 2019, **295**, 1067-1074.
- 9 H. Zhang, Q. Qi, P. G. Zhang, W. Zheng, J. Chen, A. G. Zhou, W. B. Tian, W. Zhang and Z. M. Sun, *ACS Applied Energy Materials*, 2018, **2**, 705-714.
- 10 X. W. Wang, C. H. Yang, X. H. Xiong, G. L. Chen, M. Z. Huang, J. H. Wang, Y. Liu, M. L. Liu and K. Huang, *Energy Storage Mater.*, 2019, **16**, 344-353.
- 11 J. J. Song, X. Guo, J. Q. Zhang, Y. Chen, C. Y. Zhang, L. Q. Luo, F. Y. Wang and G. X. Wang, *J. Mater. Chem. A*, 2019, **7**, 6507-6513.